Proceedings of GT2007
ASME Turbo Expo 2007: Power for Land, Sea and Air
May 14-17, 2007, Montreal, Canada

GT2007-27814

STATIC AND DYNAMIC CHARACTERISTICS OF AIR FOIL THRUST BEARING CONSIDERING TILTING PAD CONDITION

Dong-Jin Park, Yong-Bok Lee, Chang-Ho Kim
Korea Institute of Science and Technology
Tribology Research Center
Seoul, 136-791, Republic of Korea
djpark@kist.re.kr, lyb@kist.re.kr, kimch@kist.re.kr

Gun-Hee Jang
Hanyang University,
Dept. of Mechanical Engineering,
Seoul, 133-791, Republic of Korea
ghjang@hanyang.ac.kr

ABSTRACT

The thrust pad of the rotor is used to sustain the axial force generated due to the pressure difference between the compressor and turbine sides of turbomachinery such as the gas turbines and turbochargers. Furthermore, this thrust pad has a role to maintain and determines the attitude of the rotor. In a real system, it also helps reinforce the stiffness and damping of the journal bearing. This study was performed for the purpose of analyzing the characteristics of the air foil thrust bearing. The model for the air foil thrust bearing used in this study is composed of two parts: one is an inclined plane, which plays a role to increase the load carrying capacity using the physical wedge effect, and the other is a flat plane. This study mainly consists of three parts. First, the static characteristics were obtained over the region of the thin air film using the finite difference method (FDM) and the bump foil characteristics using the finite element method (FEM). Second, the analysis of the dynamic characteristics was conducted by perturbation method. For more exact calculation, the rarefaction gas coefficients perturbed about the pressure and film thickness were taken into consideration. At last, the static and dynamic characteristics of the tilting condition of the thrust pad were obtained. Furthermore, the load carrying capacity and torque were calculated for both tilting and not-tilting conditions. From this study, several results were presented: 1) the stiffness and damping of the bump foil under the condition of the various bump parameters, 2) the load carrying capacity and bearing torque at the tilting state, 3) the bearing performance under various bearing parameters, 4) the effects considering the rarefaction gas coefficients.

Keyword: Air foil bearings; Thrust pad; Tilting condition; Perturbation method.

INTRODUCTION

The operation of the rolling element and oil-lubricated sliding bearings is limited in high temperatures and speeds; therefore, the tension dominated foil bearing was proposed as the alternative [1]. But it had the shortcoming of low load carrying capacity; therefore in order to increase the load carrying capacity, several types of foil bearing have been devised. The 1st generation air foil bearing which is analyzed in this study mainly consists of corrugated bump foil with flexibility and flat top foil with a role to generate the lubricated air film. This flexible structure settles the critical problems due to the sudden disturbance, thermal expansion of the rotor and large foreign particles and provides stability with sufficient damping capacity. With those advantages, many analytic and experimental studies to apply the air foil bearing to turbomachinery have been executed.

First, Walowit and Anno analytically calculated the structural stiffness of the bump using the circular beam equation concerning the inner mounted bump by assuming the plane strain theory [2]. The bump stiffness equation suggested in that study didn't consider the friction effect between the bumps and housing or bumps and top foil. Also, Heshmat et al. numerically analyzed the bump foil bearing by using Walowit's equation for bump stiffness [3]. In that study, it was assumed that the bump foil is an elastic foundation and used the compressible Reynolds equation about thin air film between the journal and the top foil. Inaddition, the load carrying capacity and bearing loss torque were calculated using the finite difference method. The authors verified that bump foil bearings have greater load carrying capacity than air bearings under the same air film thickness. Carpino and Peng investigated the static characteristics of bump foil bearing by using the FEM [4]. The authors compared both results using FEM and FDM and verified that FEM results were identical to FDM results. They also calculated the damping coefficient of the bump foil using equivalent viscous damping derived from energy dissipation principles [5]. Furthermore, the authors calculated the dynamic characteristics using these damping components. In that study, the equivalent viscous damping for the Coulomb damping was calculated by equating the energy dissipated in a cycle of journal excitation. The paper verified that this equivalent viscous damping component increases the overall stiffness and damping of the bump foil bearing. Heshmat and Ku calculated structural stiffness using analytical methods and compared them with the experimental results. From this examination, the authors verified that the stiffness of each bump is different due to the interaction between the bumps [6]. Lee et al. calculated the characteristics of the air foil journal bearing considering the slip flow effect and verified that the load

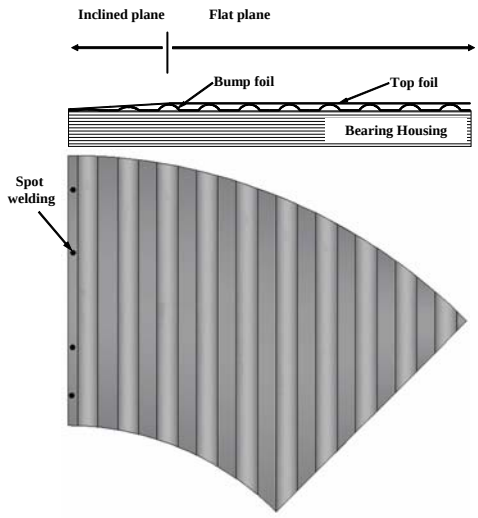

Figure 1. The configuration of the air foil thrust bearing

carrying capacity decreases compared with the no-slip boundary condition [7]. San Andres and Kim analyzed air foil bearing considering a structural loss factor, exemplifying the dry-friction damping capacity of the underlying foil-bump strip structure, and verified that it enhances the damping ability of air foil bearings [8].

Despite the existence of many studies on the analysis of air foil journal bearing, the study of air foil thrust bearing is out of fashion. Yet as the operating speed of the turbomachiney and the axial force due to the pressure difference between the turbine and compressor sides gradually have increased, studies with the purpose of increasing the load carrying capacity of the air foil thrust bearing are in progress. Bruckner designed the top foil as the shell model using bi-harmonic function and obtained the static characteristics considering the thermal effects [9]. Heshmat et al. calculated the displacement and deformation of the bump foils using FEA modeling for the foil thrust bearing [10]. The authors also analyzed the air foil thrust bearing using the finite difference method and showed that the optimized geometry for a bearing is as follows: θ_e = 45 deg, β = 1 [11]. In addition, it was presented that the inclined plane of the thrust bearing (see Fig. 1) plays an important role in generating the pressure gradient. Iordanoff [12,13] proposed the equation for the local bump compliance. Using those results, he calculated the overall static characteristics. Recently, experimental research has mainly been undertaken [14,15]. But those former works didn't consider the tilting condition and axial movement of the rotor. Also, the important parameters needed to obtain the rotor characteristics versus the rotating speed, the dynamic characteristics, were not referred to in previous works. Thus, this paper was written with the purpose of obtaining the dynamic characteristics and the bearing performance variation at tilting condition.

This analysis was based on the finite different method using the cylindrical coordinates. For more exact solutions, the bump foil was calculated by the finite element method suitable to the structure analysis. Because the position of the bump foil is not suitable for the cylindrical coordinates, the process to fit the FEM grids to the FDM grids was preceded. One bump foil acts under the correlation among the several bumps and the static and dynamic characteristics are determined by the pressure distribution and bump number [16]. Also, in the bump foil FEM analysis, the reacting force at both sides of a bump was taken into consideration, calculated, and introduced to the overall air foil thrust bearing analysis. The rarefaction coefficients are dependent on the temperature, pressure, and film thickness. The rarefaction coefficients perturbed about the pressure and film thickness were calculated using the equation proposed in the literature [17]. Finally, those coefficients were used to calculate the bearing static and dynamic characteristics.

NOMENCLATURE

b_i	Bump width at ith bump [m]
c	Thrust pad initial clearance [m]
e	Thrust pad eccentricity [m]
h	Air film thickness [m]
r_i	Bearing inner radius [m]
r_o	Bearing outer radius [m]
u_r	Linear velocity to the radial direction[m/sec]
u_θ	Linear velocity to the angular direction [m/sec]
υ	Whirl frequency [1/sec]
w	Angular velocity [rad/sec]
Bn	The number of bump
C_e	Bump damping [N·sec/m]
C	The damping coefficient of the air foil bearing [N·sec/m]
D_{gas}	The diameter of the gas molecule ~0.3 nm
F_i	Concentrated force on the top of the bump [N]
$F_{a,i}$	Vertical reacting force on the left side of ith bump [N]
$F_{b,i}$	Vertical reacting force on the right side of ith bump [N]
H	Bump foil height [m]
H_1	Height difference between inclined and flat planes [m]
K	The stiffness of the air foil bearing [N/m]
K_e	Bump stiffness [N/m]
L_b	Length of a bump [m]
N_A	Avogadro's number ~6.02×10^{23}
P	Pressure [N/m^2]
P_a	Ambient pressure ~1.014×10^5 [N/m^2]
P_b	Peach of a bump [m]
T	Bearing torque [N·m]
W	Bearing load [N]
r, θ	Cylindrical coordinates
X, Y, Z	Rectangular coordinates
ΔP	Perturbed pressure [N/m^2]
$\Delta\omega$	Perturbed bump deflection [m]
Kn	Knudsen number
α	Bump foil compliance
β	The ratio of the inclined plane to flat plane
ε	Thrust pad eccentricity
δ	Bump foil deflection [m]
μ	Viscosity of air [N·sec/m^2]
θ_e	One pad angle [deg]
$\theta_{e,Z}$	The tilting angle about the Z axes [deg]
$\theta_{e,Y'}$	The tilting angle about the Y' axes [deg]
η	Friction coefficient between bump and bearing housing
ψ	Friction coefficient between bump and top foil
λ	The mean free path of the gas [m]
φ^p	Rarefaction gas constant
γ	Whirl frequency ratio
Λ	Bearing number

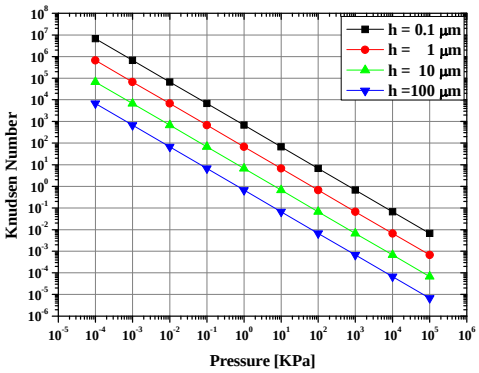

Figure 2. Knudsen number of thin air film in constant temperature, 300K

THIN AIR FILM ANAYSIS THEORY

Modified Reynolds Equation

When the Knudsen number is between 0.01 and 10, it can be assumed that the flow is the slip flow and the medium gas is the rarefaction gas. The film thickness of the air foil bearing is normally in the 10 ~ 50 μm range as can be seen in the analysis of the rarefaction gas from Fig. 2. The modified Reynolds equation can be derived from the continuity equation and Navier-stoke equation using the 1st order slip boundary condition as follows:

$$u_r(z=0) = \lambda \left.\frac{\partial u_r}{\partial z}\right|_{z=0} \tag{1}$$

$$u_r(z=h) = -\lambda \left.\frac{\partial u_r}{\partial z}\right|_{z=h} \tag{2}$$

$$u_\theta(z=0) = wr + \lambda \left.\frac{\partial u_r}{\partial z}\right|_{z=0} \tag{3}$$

$$u_\theta(z=h) = -\lambda \left.\frac{\partial u_r}{\partial z}\right|_{z=h} \tag{4}$$

The obtained radial and angular velocity of the flow are as follows:

$$u_r = -\frac{1}{2\mu}\frac{\partial P}{\partial r}\left(h\lambda + hz - z^2\right) \tag{5}$$

$$u_\theta = -\frac{1}{2\mu r}\frac{\partial P}{\partial \theta}\left(h\lambda + hz - z^2\right) + wr\left(1 - \frac{z+\lambda}{h+2\lambda}\right) \tag{6}$$

Introducing both velocity terms to the continuity equation, the modified Reynolds equation can be obtained from the following equations:

$$\frac{\partial}{\partial r}\left\{r\frac{\rho h^3}{12\mu}\varphi^P\frac{\partial P}{\partial r}\right\} + \frac{1}{r}\frac{\partial}{\partial \theta}\left\{\frac{\rho h^3}{12\mu}\varphi^P\frac{\partial P}{\partial \theta} - \frac{\rho h\left(wr^2\right)}{2}\right\} = \frac{\partial}{\partial t}\left(\rho h r\right) \tag{7}$$

Here, φ^P represents the rarefaction coefficients and is as follows:

$$\varphi^P = 1 + 6\frac{\lambda}{h} = 1 + 6Kn \tag{8}$$

Each variable can be normalized using typical parameters. The normalized form of the modified Reynolds equations is as follows:

$$\frac{\partial}{\partial \bar{r}}\left\{\bar{r}\bar{P}\bar{h}^3\left(1+6Kn\right)\frac{\partial \bar{P}}{\partial \bar{r}}\right\} + \frac{1}{\bar{r}}\frac{\partial}{\partial \theta}\left\{\bar{P}\bar{h}^3\left(1+6Kn\right)\frac{\partial \bar{P}}{\partial \theta}\right\} = 2\Lambda\gamma\frac{\partial\left(\bar{P}\bar{h}\bar{r}\right)}{\partial \bar{t}} + \Lambda\frac{\partial}{\partial \theta}\left(\bar{P}\bar{h}\bar{r}\right) \tag{9}$$

Where, $\bar{r} = r / r_o$, $\bar{h} = h / c$, $\bar{t} = t\upsilon$ and $\bar{P} = P / P_a$. Also, γ is whirl frequency ratio (υ/w) and Λ is the bearing number.

$$\Lambda = \frac{6\mu w R^2}{P_a c^2} \tag{10}$$

Air Film Thickness Calculation

The simplified 1 DOF system with stiffness and damping is used for calculating the film thickness. The magnitude of the bump deflection changes with the magnitude of the pressure, and the related equation is as follows:

$$\bar{P} - 1 = \bar{K}_e\bar{\delta} + \bar{C}_e\gamma\frac{d\bar{\delta}}{d\bar{t}} \tag{11}$$

Here, $\bar{K}_e$ and $\bar{C}_e$ represent normalized stiffness and damping coefficients of the bump foil as follows: $K_e c/P_a$ and $C_e cw/P_a$, respectively.

The normalized film thickness can be calculated using the above equation of the bump foil deflection and is as follows:

$$\bar{h} = 1 - \varepsilon + \left(r/e\right)\cos\left(\varphi - \theta_{e,Z}\right)\sin\left(\theta_{e,Y'}\right) + \bar{\delta} \tag{12}$$

when $-\pi/2 + \theta_{e,Z} < \varphi \le \pi/2 + \theta_{e,Z}$

$$\bar{h} = 1 - \varepsilon - \left(r/e\right)\cos\left(\varphi - \theta_{e,Z}\right)\sin\left(\theta_{e,Y'}\right) + \bar{\delta} \tag{13}$$

when $\pi/2 + \theta_{e,Z} < \varphi \le 3\pi/2 + \theta_{e,Z}$

where, $\theta_{e,z}$ and $\theta_{e,Y'}$ represent the tilting angle about the Z and Y' axes, respectively. The angles are determined from the eccentricities at both journals. Figures 3 and 4 show those variables. Also, $\bar{\delta}$ is the normalized bump foil deflection under pressure which acts on the top foil.

$$\bar{\delta} = \alpha\left(\bar{P} - 1\right) \tag{14}$$

Here, α represents the compliance of the bump foil, inverse proportional to the bump foil stiffness.

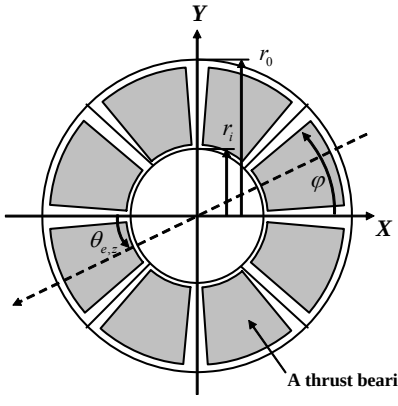

Figure 3. Brief configuration of the air foil thrust bearing

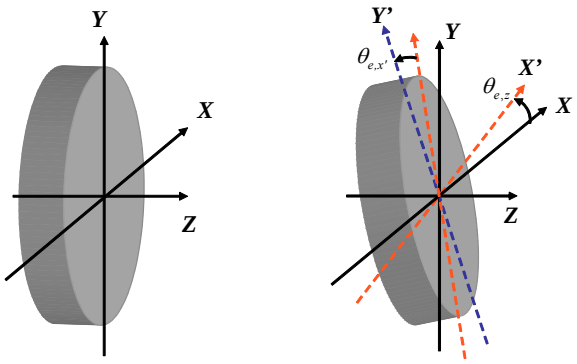

Figure 4. Tilting condition of thrust pad due to the eccentricity of the rotating journal

Tilting Pad Condition

When the thrust pad tilts, more load acts on the area at which the film thickness decreases. Moreover, it affects the attitude of the rotating journal with a non-symmetric shape of both sides. So, the load calculation at each degree of angle is necessary to calculate the eccentricity until it converges to any value satisfying the force and momentum equilibrium state. Figure 4 shows the thrust pad at steady state and tilting condition. When the eccentricity is generated at both journal parts non-uniformly, the tilting generates. The $\theta_{e,Z}$ is the equivalent eccentricity line and $\theta_{e,Y'}$ presents the tilting angle.

Perturbation Method

The dynamic operating regime is traditionally described as a small amplitude motion of the rotor about an equilibrium position. For displacement perturbation, the film thickness, h, is described in following equations:

$$\overline{h_0} + \overline{h_z}\Delta z + \overline{h_{\dot z}}\Delta \dot z = 1 - \varepsilon - \Delta z - \Delta \dot z + \frac{r}{c}\cos(\varphi - \theta_{e,Z})\sin(\theta_{e,Y'}) + \left(\overline{\delta_0} + \overline{\delta_z}\Delta z + \overline{\delta_{\dot z}}\Delta \dot z\right) \quad \text{when, } -\pi/2 + \theta_{e,Z} < \varphi \le \pi/2 + \theta_{e,Z} \tag{15}$$

$$\overline{h_0} + \overline{h_z}\Delta z + \overline{h_{\dot z}}\Delta \dot z = 1 - \varepsilon - \Delta z - \Delta \dot z - \frac{r}{c}\cos(\varphi - \theta_{e,Z})\sin(\theta_{e,Y'}) + \left(\overline{\delta_0} + \overline{\delta_z}\Delta z + \overline{\delta_{\dot z}}\Delta \dot z\right) \quad \text{when, } \pi/2 + \theta_{e,Z} < \varphi \le 3\pi/2 + \theta_{e,Z} \tag{16}$$

And the perturbed pressure is as follows:

$$\overline{P_o} + \overline{P_z}\Delta z + \overline{P_{\dot z}}\Delta \dot z - 1 = \overline{K_e}\left(\overline{\delta_0} + \overline{\delta_z}\Delta z + \overline{\delta_{\dot z}}\Delta \dot z\right) + \overline{C_e}\gamma\frac{d}{dt}\left(\overline{\delta_0} + \overline{\delta_z}\Delta z + \overline{\delta_{\dot z}}\Delta \dot z\right) \tag{17}$$

where, ΔP and $\Delta\omega$ represent perturbed pressure and deflection, respectively, and are as follows:

$$\Delta P = P_z\Delta z + P_{\dot z}\Delta \dot z \tag{18}$$

$$\Delta \delta = \delta_z\Delta z + \delta_{\dot z}\Delta \dot z \tag{19}$$

To apply the perturbation method to the Knudsen number, the following equations regarding the Knudsen number were used [16]:

$$\mathrm{Kn} = \frac{RT}{\pi\sqrt{2}d_{gas}^2 N_A P h} \tag{20}$$

The Knudsen number is a variable related with pressure, film thickness and environment temperature. In this study, the fixed temperature, 300K, was assumed. As well, it was regarded as a variable related to pressure and film thickness. The equation is as follows:

$$\mathrm{Kn}(P,h) = \frac{C_1}{Ph} \tag{21}$$

where, C_1 is 6.7×10^{-2}. The rarefaction coefficient is as follows:

$$\varphi^P = \varphi^P{}_0 + \left(\frac{\partial\varphi^P}{\partial P}\right)_0\Delta p + \left(\frac{\partial\varphi^P}{\partial h}\right)_0\Delta h \tag{22}$$

Here, the perturbed rarefaction coefficients in terms of pressure and film height can be expressed as follows:

$$\left(\frac{\partial\varphi^P}{\partial P}\right) = -\frac{0.402}{P^2 h}, \quad \left(\frac{\partial\varphi^P}{\partial h}\right) = -\frac{0.402}{Ph^2} \tag{23}$$

Using the perturbed variables, the modified Reynolds equation can be divided into a zeroth-order equation and two first-order equations ($\Delta\bar z$ and $\Delta\dot{\bar z}$ terms). Those are as follows:

Zeroth-order equation,

$$\frac{\partial}{\partial\bar r}\left\{\bar r\overline{P_o h_o}^3\varphi_o{}^P\frac{\partial\overline{P_o}}{\partial\bar r}\right\} + \frac{1}{\bar r}\frac{\partial}{\partial\theta}\left\{\overline{P_o h_o}^3\varphi_o{}^P\frac{\partial\overline{P_o}}{\partial\theta}\right\} = \Lambda\frac{\partial}{\partial\theta}\left(\overline{P_o h_o}\bar r\right) \tag{24}$$

First-order equation,

$\Delta\bar z$ *term;*

$$\frac{\partial}{\partial\bar r}\left\{\begin{array}{l}\bar r\overline{P_0 h_0}^3\varphi_0{}^P\frac{\partial\overline{P_z}}{\partial\bar r} + \bar r\overline{P_z h_0}^3\varphi_0{}^P\frac{\partial\overline{P_0}}{\partial\bar r} + 3\bar r\overline{P_0 h_0}^2\overline{h_z}\varphi_0{}^P\frac{\partial\overline{P_0}}{\partial\bar r} + \\ \overline{P_0 h_0}^3\left(\frac{\partial\varphi^P}{\partial P}\right)_0\overline{P_z}\frac{\partial\overline{P_0}}{\partial\bar r} + \bar r\overline{P_0 h_0}^3\left(\frac{\partial\varphi^P}{\partial h}\right)_0\overline{h_z}\frac{\partial\overline{P_0}}{\partial\bar r}\end{array}\right\} + \frac{1}{\bar r}\frac{\partial}{\partial\theta}\left\{\begin{array}{l}\overline{P_0 h_0}^3\varphi_0{}^P\frac{\partial\overline{P_z}}{\partial\theta} + \overline{P_z h_0}^3\varphi_0{}^P\frac{\partial\overline{P_0}}{\partial\theta} + 3\overline{P_0 h_0}^2\overline{h_z}\varphi_0{}^P\frac{\partial\overline{P_0}}{\partial\theta} + \\ \overline{P_0 h_0}^3\left(\frac{\partial\varphi^P}{\partial P}\right)_0\overline{P_z}\frac{\partial\overline{P_0}}{\partial\theta} + \overline{P_0 h_0}^3\left(\frac{\partial\varphi^P}{\partial h}\right)_0\overline{h_z}\frac{\partial\overline{P_0}}{\partial\theta}\end{array}\right\} = \Lambda\bar r\frac{\partial}{\partial\theta}\left(\overline{P_z h_0} + \overline{P_0 h_z}\right) - 2\Lambda\gamma\bar r\left(\overline{P_z h_0} + \overline{P_0 h_z}\right) \tag{25}$$

$\Delta\dot{\bar z}$ *term;*

$$\frac{\partial}{\partial\bar r}\left\{\begin{array}{l}\bar r\overline{P_0 h_0}^3\varphi_0{}^P\frac{\partial\overline{P_{\dot z}}}{\partial\bar r} + \bar r\overline{P_{\dot z} h_0}^3\varphi_0{}^P\frac{\partial\overline{P_0}}{\partial\bar r} + 3\bar r\overline{P_0 h_0}^2\overline{h_z}\varphi_0{}^P\frac{\partial\overline{P_0}}{\partial\bar r} + \\ \overline{P_0 h_0}^3\left(\frac{\partial\varphi^P}{\partial P}\right)_0\overline{P_z}\frac{\partial\overline{P_0}}{\partial\bar r} + \bar r\overline{P_0 h_0}^3\left(\frac{\partial\varphi^P}{\partial h}\right)_0\overline{h_z}\frac{\partial\overline{P_0}}{\partial\bar r}\end{array}\right\} + \frac{1}{\bar r}\frac{\partial}{\partial\theta}\left\{\begin{array}{l}\overline{P_0 h_0}^3\varphi_0{}^P\frac{\partial\overline{P_{\dot z}}}{\partial\theta} + \overline{P_{\dot z} h_0}^3\varphi_0{}^P\frac{\partial\overline{P_0}}{\partial\theta} + 3\overline{P_0 h_0}^2\overline{h_z}\varphi_0{}^P\frac{\partial\overline{P_0}}{\partial\theta} + \\ \overline{P_0 h_0}^3\left(\frac{\partial\varphi^P}{\partial P}\right)_0\overline{P_z}\frac{\partial\overline{P_0}}{\partial\theta} + \overline{P_0 h_0}^3\left(\frac{\partial\varphi^P}{\partial h}\right)_0\overline{h_z}\frac{\partial\overline{P_0}}{\partial\theta}\end{array}\right\} = \Lambda\bar r\frac{\partial}{\partial\theta}\left(\overline{P_{\dot z} h_0} + \overline{P_0 h_{\dot z}}\right) + 2\Lambda\gamma\bar r\left(\overline{P_{\dot z} h_0} + P\overline{h_z}\right) \tag{26}$$

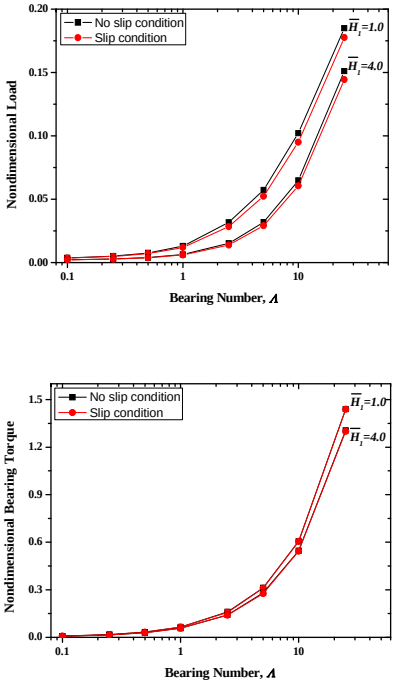

Figure 5. Nondimensional bearing static characteristics considering slip flow and no slip flow condition at bump foil compliance; α = 0.1 and eccentricity; ε = 0.6

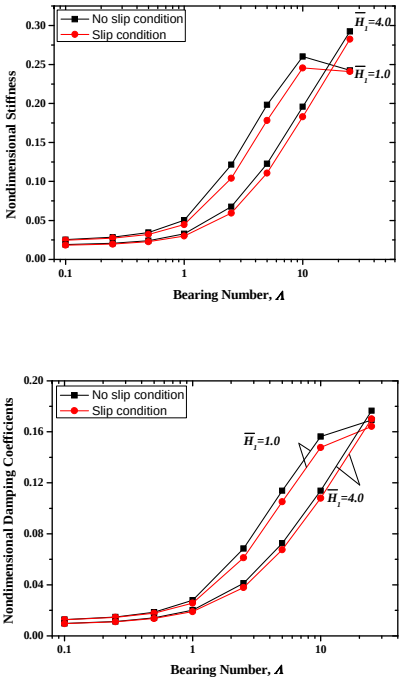

Figure 6. Nondimensional bearing dynamic characteristics considering slip flow and no slip flow conditions with bump foil compliance; α = 0.1, eccentricity; ε = 0.6, bump foil stiffness; $\bar{K}_e$ =25 and bump foil damping coefficients; $\bar{C}_e / w$ =2.5 x 10^{-2}

Here, perturbed film thickness can be derived from Equations 13-15 and those are as follows:

$$\bar{h}_{\bar{z}} = \frac{\bar{K}_e\left(\bar{P}_x - \bar{K}_e\right) + \bar{C}_e\gamma\left(\bar{P}_{\dot{x}} - \bar{C}_e\gamma\right)}{\bar{K}_e^2 + \left(\bar{C}_e\gamma\right)^2}, \quad \bar{h}_{\bar{z}} = \frac{\bar{K}_e\left(\bar{P}_{\dot{x}} - \bar{K}_e\right) - \bar{C}_e\gamma\left(\bar{P}_x + \bar{C}_e\gamma\right)}{\bar{K}_e^2 + \left(\bar{C}_e\gamma\right)^2} \tag{27}$$

Note that the bump foil stiffness and damping decrease the perturbed film thickness.

Static Characteristics Analysis

The static pressure and film thickness are calculated using the finite difference method with 105 grids to the angular direction and 45 grids to the radial direction until the values of the pressure at all grid points converge using the SUR (Successive Under Relaxation) method. The load and torque can be obtained along with the pressure and film thickness. Those can be expressed as the following equations:

$$\bar{W} = \iint_A \bar{P}_0 \bar{r} d\theta d\bar{z}, \ \bar{W} = W / P_a r_o^2 \tag{28}$$

$$\bar{T} = \iint_A \left[\frac{\bar{r}\bar{h}}{2}\left(\frac{\partial \bar{P}_0}{\partial \theta}\right) + \frac{\mu \bar{r}^3 w}{\bar{h}} \right] d\theta d\bar{z}, \quad \bar{T} = T / c P_a r_o^2 \tag{29}$$

Figure 5 shows the analysis results of the static characteristics. Two conditions, slip flow and no slip flow, were taken into consideration to confirm the slip flow effect. In the case of load carrying capacity, the results with the slip flow condition have low values at overall bearing numbers. This is because the hydrodynamic pressure decreases due to decreased linear velocity at both walls with the slip flow condition. The bearing torque also had the same trends but the difference magnitude was less than those of the load carrying capacity. Futher, as the gradient of the inclined plane decreases, the static characteristics increase.

Dynamic Characteristics Analysis

The dynamic characteristics, stiffness and damping coefficients are calculated from perturbed pressure. Similarly with static characteristics analysis, the SUR method was used for stable convergence. In this study, only the coefficients to the radial direction under the perturbation to the radial direction, direct term, were taken into consideration. Those can be expressed as the following equations:

$$\bar{K}_{zz} = \iint_A \bar{P}_{\bar{z}} d\theta d\bar{z}, \ \bar{K}_{zz} = K_{zz} / P_a R^2 \tag{30}$$

$$\bar{C}_{zz} = \iint_A \bar{P}_{\dot{\bar{z}}} d\theta d\bar{z}, \ \bar{C}_{zz} = C_{zz} w / P_a R^2 \tag{31}$$

Figure 6 presents the stiffness and damping coefficients under two conditions. Similarly with the static characteristics, the results with slip flow condition were less than those with no slip flow condition. Furthermore, trends indicating that both results decrease at high bearing numbers were confirmed. Figure 8 shows the stiffness and damping coefficients of the air foil thrust bearing with various structural stiffness coefficients of the bump foil. When the structural stiffness increases, both the dynamic coefficients increase. Yet in the case of Fig. 9, the damping coefficients of the air foil thrust bearing decrease as the structural damping increases. It is

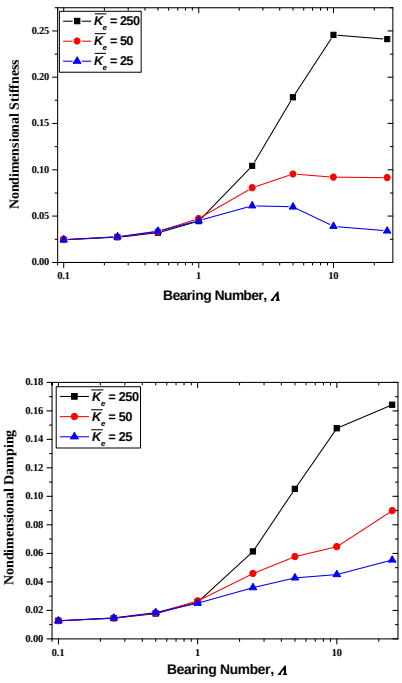

Figure 7. Dynamic characteristics of bump foil thrust bearing at various bump stiffness when ε is 0.6 and $\bar{C}_e / w$ =2.5 x 10^{-2}

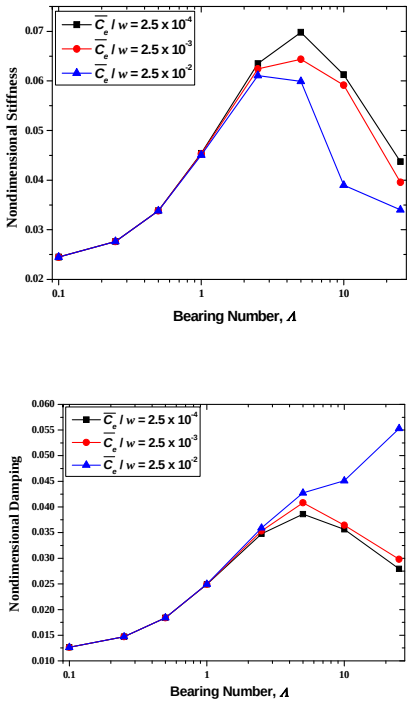

Figure 8. Dynamic characteristics of bump foil thrust bearing at various bump damping coefficients when ε is 0.6 and $\bar{K}_e$ =25

because $\bar{h}_z$ increases regardless of whether $\bar{h}_z$ decreases when the bump foil structural damping increases. There results can be checked from Equation (27) for the perturbed film thickness.

BUMP FOIL ANALYSIS

Heshmat et al. [10] verified that the case with eight pads, where each pad consists of 45 , has optimum performance. Here, the inclined plane of each pad generates more pressure. Recently, the air foil thrust bearing divided into eight thrust pads, at 90 , has been studied. Figure 9 shows one thrust bearing configuration. The inclined part height is able to be adjusted by putting several foil sheets between bump and top foil or using the various bump foil heights. Similar to the effect of the height difference between inclined and flat planes, the angle ratio (the angle of inclined plane/the flat plane) is an important parameter. The air foil thrust bearing with a configuration where the angle ratio is smaller can achieve greater then more load carrying capacity (see the results of Fig. 5 and 6). In this chapter, analysis on the bump foil of the air foil thrust bearing which has 8 pads and an angle ratio of one was executed. As well, the boundary with the spot welding point of Fig. 1 is regarded as a fixed end and the other boundary as a free end.

Bump Foil Modeling

Figure 10 shows one bump foil model with two cases of boundary conditions. The deformations due to the normal force acted on the top touched with the top foil are variable to the constraint condition at both ends of a bump. Figure 10(a) presents the bump at the fixed end side. The left end plays a role to prevent the displacement to both the vertical and horizontal direction, and the displacement of the other end is determined by the friction coefficient and normal force, F_b. On the contrary, Fig. 10(b) shows the bump model with both free ends, which are constrained by the state of related bumps. The methods to analyze the interaction among bumps are divided into two cases: one is designed to analyze each bump and couple all the analysis results using the interacting force [15], and the other is designed to calculate the overall bumps simultaneously. The former method is suitable to the bump foil analysis with more than 20 bumps for time saving regarding numerical scheme. But in order to obtain the internal forces for the purpose of comparison with the friction forces at both points of a bump, the stiffness matrix has to be transformed to an inverse

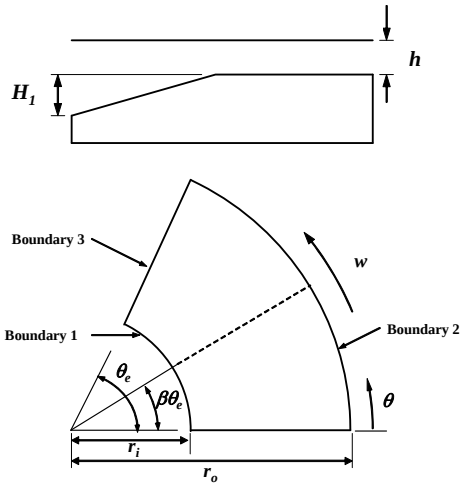

Figure 9. A thrust bearing schematics, H_1: the height of the inclined plane, $\beta\theta_e$: the angle occupied with the inclined plane

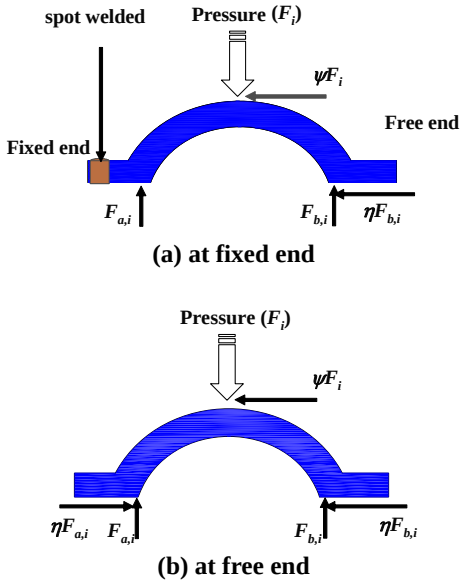

Figure 10. One bump model configuration

matrix form twice. Thus, methods which calculate the displacements of overall bump elements are adaptable to bump foil analysis with bumps under 15 for a simple numerical scheme because they don't need to obtain the internal forces. The number of bumps for the thrust bearing analysis is approximately ranged from 6 to 12 according to the bump foil and thrust pad sizes. So, the latter method, the stiffness matrix measuring 1536 × 1536 (8 bumps; 64 elements for each bump; transverse and horizontal deflections, and bending), was selected.

As the preceding process to calculate the structural stiffness and damping of bumps demonstrated, the bump widths which are important parameter to determine the value of the structural characteristics were obtained. It is expected that the characteristics increase as the bump width increases. The bump widths can be calculated from the following equations:

$$b_i = \sqrt{r_o^2 - (P_b \times i)^2} - \sqrt{r_i^2 - (P_b \times i)^2} \qquad \text{at } i=1 \sim Bn1 \quad (32)$$

$$b_i = \sqrt{r_o^2 - (P_b \times i)^2} - P_b \times i / \sin\theta_e \qquad \text{at } i=Bn1+1 \sim Bn \quad (33)$$

Here i and $Bn1$ represent ith bump and the number of bumps which meet at boundary 1 in Fig. 9.

Table 1. The parameters for the bump analysis

Parameters	Values
Inner raidius (r_o)	0.05 m
Outer radius (r_i)	0.025 m
Foil thickness (t)	0.1 mm
Bump length (L_b)	3.0 mm
Bump height (H)	0.5 mm
Friction coefficients (ψ, η)	0.2
Exciting frequency	1,000 Hz

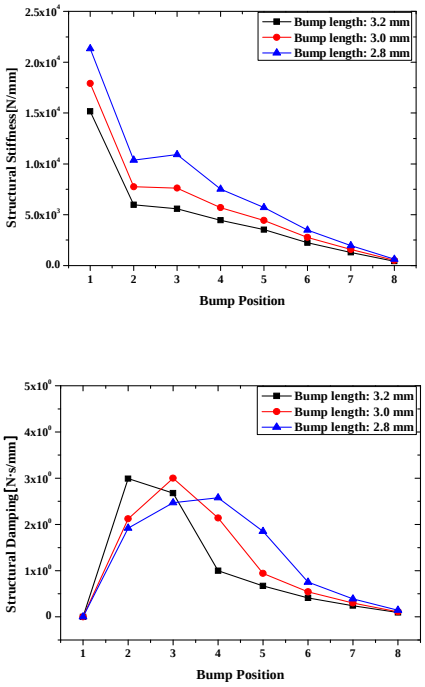

Figure 11. Structural stiffness and damping of bump foil with various bump lengths under uniform loads

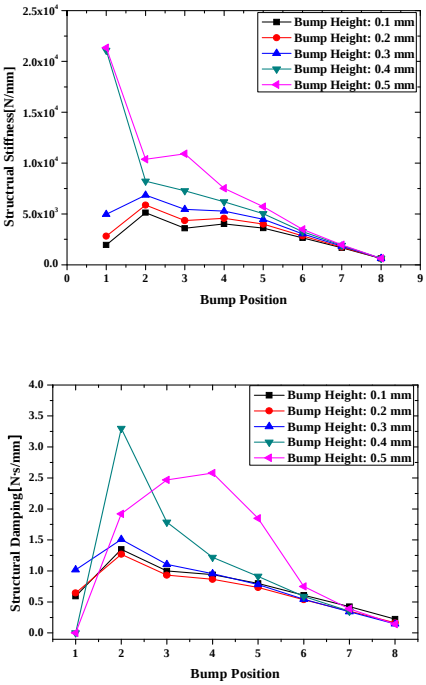

Figure 12. Structural stiffness and damping of bump foil with various bump heights under uniform loads

Numerical Scheme for Bump Foil Analysis

For the analysis method, the finite element method suitable to structure analysis was conducted. A bump model was divided into two dimensional 64 elements with widths variable to the element position to save calculating time. Because the number of bumps is determined from the bump foil parameters, bump pitch, bearing inner radius, outer radius and one pad angle, an analysis to determine the number was conducted. Additionally, bearing performances under various loads were calculated. For damping coefficients, the energy dissipation equation using the dry friction was used [5]. The equivalent Coulomb damping can be expressed as follows:

$$C_{eq} = \frac{4\eta F_{L,i}}{\pi\omega\delta_{L,x}} + \frac{4\eta F_{R,i}}{\pi\omega\delta_{R,x}} \tag{34}$$

Here, δ_{Lx}, *and* $\delta_{R,x}$ represent the horizontal deflections of the bump foil at the point at which the bump is touched with top foil and bearing housing, respectively.

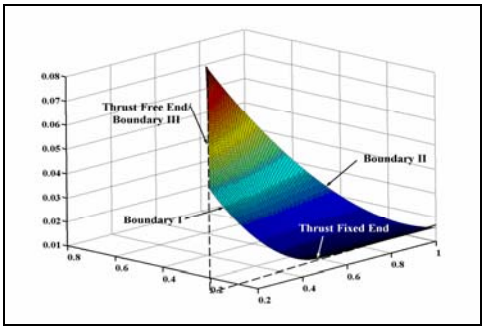

Figure 13. Compliance of a thrust bearing pad

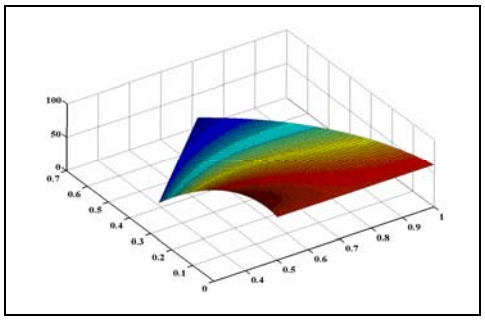

Figure 14. Non-dimensional stiffness coefficients

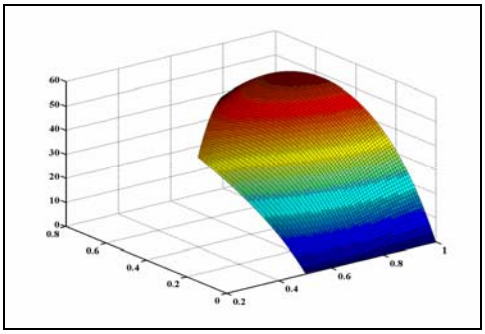

Figure 15. Non-dimensional damping coefficients

Table 2. The parameters of the bump foil used for the air foil thrust bearing analysis

Parameters	Values
Inner radius (r_o)	0.1 m
Outer radius (r_i)	0.05 m
Foil thickness (t)	0.1 mm
Bump length (L_b)	3.0 mm
Bump height (H)	0.5 mm
Bump pitch (P_b)	7.0 mm
The number of bumps	11
Friction coefficients (ψ, μ)	0.2
Angle of inclined part	22.5
Total pad number	8

Results of Numerical Analysis

When the friction forces, $\eta F_{L,i}, \eta F_{R,I}$ and ψF_i(see Fig. 10), generate, those accumulate to the fixed end. When the reacting force at the end of the i^{th} bump is larger than the internal force by which the bump deforms, the bump can be supposed to have fixed boundaries at both sides. At that time, the bump has large stiffness and no damping due to no-relative displacement between bump foil and bearing housing. Figure 11 shows the stiffness and damping of the bumps in contrast with the bump length. Here, the bump pitch is the same in all cases and the bump position represents the bumps from fixed end (1) to free end (8), respectively. The variables for this analysis are presented in Table 1. The bump at the side of the fixed end has the largest stiffness. Nevertheless, the damping coefficient is zero due to no relative displacement. In this case, both the ends of the bump can be supposed to have fixed ends because the interacting force by the friction force is larger than the internal force so that the bump is deflected by the load. As well, as the bump position moves to the free end, the stiffness and damping coefficients decrease. This is because the bump width and the interacting force decrease. The results also reveal that the bump performances are inversely proportional to the bump length and the damping coefficient is proportional to the stiffness only in cases where both the ends of a bump aren't fixed. Figure 12 presents the results for the bump performance versus the bump height. As the bump height increases, the stiffness and damping increase. The overall trends are similar to the results of Fig. 11.

Calculation of Air Foil Thrust Bearing Characteristics Using Bump Analysis Results

The data of the bump foil analysis are used to obtain the pressure distribution of the air film over the top foil and dynamic characteristics using the perturbation method. Because those are discontinuous in the boundaries between bumps, the stiffness and damping coefficients were curve fitted using a polynomial equation. Figures 13 to 15 show non-dimensional coefficients curves fitted using 9~25 points. Similarly with the results of bump analysis, the stiffness decreases from the fixed end to free end. The damping coefficients also followed the same trends. The coefficients are changed by the bearing parameters and the load condition, and the calculation and curve fitting process have to be undertaken before air film analysis. For air film analysis, the perturbation method was applied to the rarefaction coefficients.

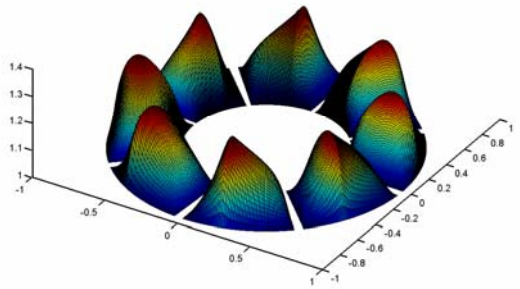

Figure 16. Pressure distribution over the 8 pad thrust pad

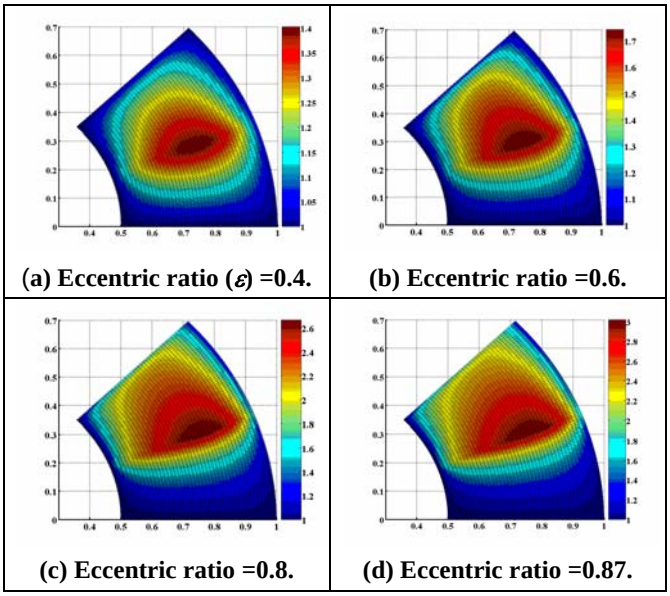

(a) Eccentric ratio (ε) =0.4. **(b) Eccentric ratio =0.6.**

(c) Eccentric ratio =0.8. **(d) Eccentric ratio =0.87.**

Figure 17. Nondimensional pressure distribution vs. the eccentricity of thrust pad at Λ=10, H_1/c=1.0

ANALYSIS RESULTS AND DISCUSSION

The numerical results obtained using the methods introduced above were based on the normalized variables. The parameters of the bump foil model used for bearing analysis are presented in Table 2. And the compliance, stiffness and damping data at all grids are the same as those of Figs. 13 to 15. Note that those values change as the bump foil parameters and pressure profiles change. Thus, in every numerical iteration process to calculate pressure of air thin film, the datum representing the bump foil characteristics have to be calculated and curve fitted. For the damping coefficients, the magnitude varies with the variation of the bearing number.

The zeroth-order equation based on the perturbation method was used for calculating the pressure distribution of thin air film, as shown in Fig. 16. Here, the z axis presents the normalized pressure, where the eccentricity was 0.2 and the ratio of the clearance, c, to H_1 was 1. Also the tilting angle was zero. Figure 17 shows the non-dimensional pressure distribution versus the eccentricity of the thrust pad. As the eccentricity increases, a high pressure region moves to the free end of the thrust pad and is broadened to both sides, where the pressure totally increases. The pressure distribution in cases where the eccentric ratio becomes 0.87 has a discontinuous region and the numerical iteration diverges. It can be supposed that the eccentric ratio is the limit for the load carrying capacity of the air foil thrust bearing. Figure 18 presents non-dimensional load versus bearing number. When the gradient of the inclined part decreases (H_1/c; i.e. $\bar{H}_1$, decreases), the load which the bearing can support increases. It is because the pressure gradient increases as the film thickness gradient decreases at the same bearing number. Figure 18(b) shows that the load increases as the eccentricity increases for the same reason as the results of Fig. 17. Generally, as the eccentric ratio increases, the load gradient versus bearing number increases.

Figure 19 shows the bearing torque versus bearing number. Because the torque is proportional to the pressure gradient and angular velocity, it increases as the bearing number increases. As was also demonstrated in Fig. 18, as the gradient of the inclined part decreases, the load which the bearing can support increases. However, the effects were less than those of the load. It is because the load magnitude is proportional to the pressure magnitude. Also, the torque is similar to the pressure gradient. As the eccentric ratio increases, the pressure is almost uniform over the post-half part of the thrust pad.

The dynamic characteristics of the air foil thrust bearing were calculated using two first-order equations, Equations (23) and (24), among the perturbation forms of a modified Reynolds equation. Both equations are coupled with each other about the perturbed

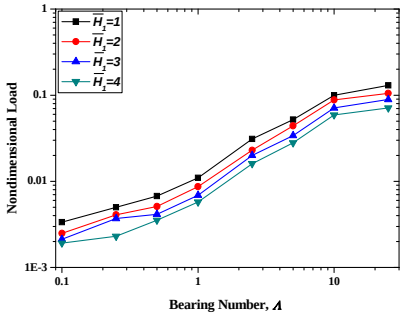

(a) Eccentric ratio=0.6

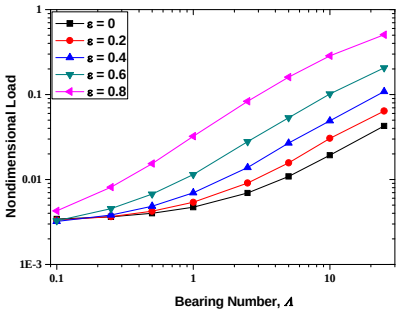

(b) H_1/c=1.0

Figure 18. Nondimensional load vs. bearing number

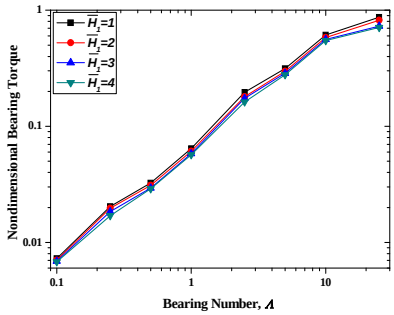

(a) Eccentric ratio =0.6

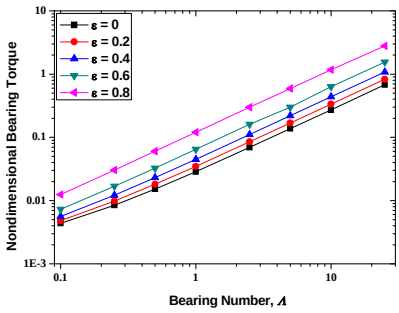

(b) H_1/c=1.0

Figure 19. Nondimensional bearing torque vs. bearing number

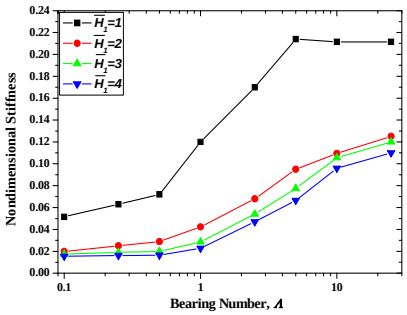

(a) Eccentric ratio =0.6

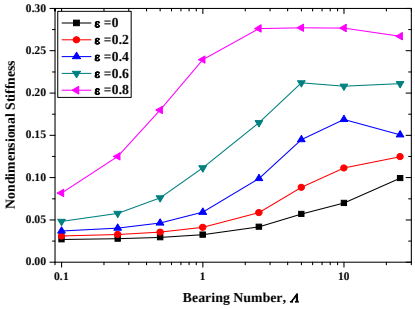

(b) H_1/c=1.0

Figure 20. Nondimensional stiffness vs. bearing number

pressure (P_z and $P_{\bar{z}}$) and perturbed film thickness (h_z and $h_{\bar{z}}$). The difference equations are calculated until each pressure term converges using the SUR method.

The results were presented in Figs. 20 and 21. Figure 20 shows the non-dimensional stiffness in the various bearing numbers, the gradients of the inclined part and the eccentric ratios. Those effects were the same as the case of load results except for the magnitudes. The damping results in Fig. 21 generally have the same trends with the stiffness. Both the coefficients had a limit at some bearing number. It is because the air foil bearing has a vibration system where two springs and two dampers (one is bump foil and the other is thin air film) are connected in series. Here, the angular velocity characteristics are dependent on those of the bump foil when the air film becomes stiff at a high bearing number. So, it can be supposed to approach the results of the values from Figs. 11 to 15.

Figure 22 shows the load and bearing torque at the condition of Λ=10, H_1/c=1.0 and ε=0.6. When the thrust pad tilts, the pressure distribution is changed due to the variation of the eccentricity. Both load and bearing torque show the trends of harmonic function versus the tilting angle about the Z axis. Also, the magnitude increases as the tilting angle about the Y' axis increases due to the increase of the film thickness variation and large eccentricity over the total pad area. In particular, at the boundary between the inclined plane and flat plane the film thickness increases (the bearing number increases), the overall dynamic gradient decreases, and high load and bearing torque generate. Figure 23 shows the pressure distribution over a pad under the tilting condition. As the tilting angle increases, high pressure generates. The distribution centre moves to the part at which the film thickness is least; i.e., the outer circumference.

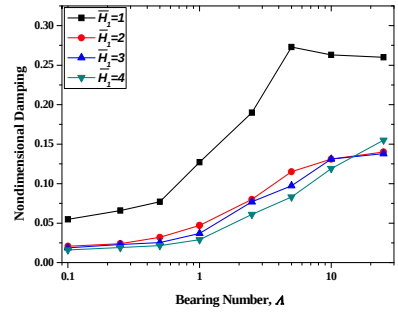

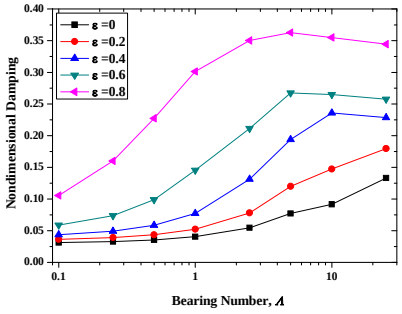

Figure 21. Nondimensional damping coefficients vs. bearing number

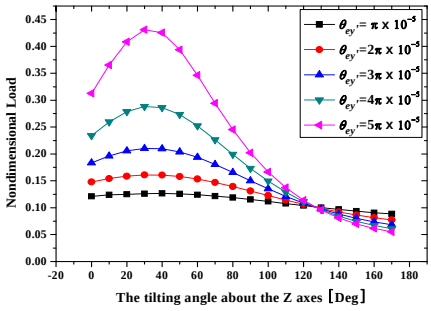

(a) Nondimensional load

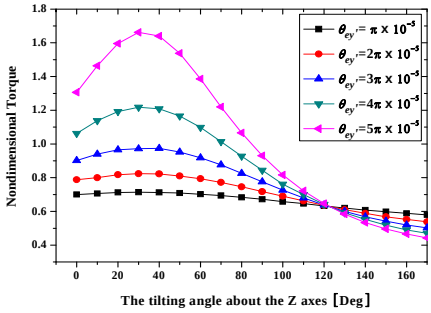

(b) Nondimensional torque

Figure 22. Nondimensional performance vs. bearing circumference

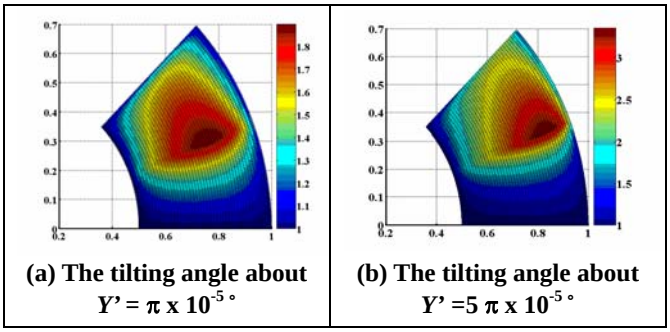

(a) The tilting angle about $Y' = \pi \times 10^{-5}$ °

(b) The tilting angle about $Y' = 5\pi \times 10^{-5}$ °

Figure 23. Pressure distribution at tilting state

CONCLUSIONS

In this study, an analysis of the air foil thrust bearing was conducted. First, the characteristics of the bump foil were analyzed using the finite element method considering the friction force between the top and bump foil, as well as the bump foil and bearing housing. In addition, using the deflection at each bump under a uniform load, the stiffness and damping were calculated. The results show that the stiffness and damping are proportional and the magnitude decreases from the fixed end to free end. The data from the bump analysis were curve fitted at several grid points to apply the characteristics of the bump foil to the overall air foil bearing analysis.

The overall air foil bearing analysis was conducted using a modified Reynolds equation with a rarefaction coefficient. Moreover, using the perturbation method, a zeroth order and two first order equations were obtained. The static pressure and perturbed pressure about the perturbed motion to the axial direction were calculated using the SUR method. The numerical results were divided into static characteristics, dynamic characteristics and the characteristics under tilting conditions. In the case of static characteristics, as the bearing number and eccentric ratio increase, the load and bearing torque increase. Also, as the gradient of the inclined part decreases, load and bearing torque increase. The dynamic characteristics, stiffness and damping coefficients, have the same trends but had a limit at some bearing number due to the characteristics of dependency to the bump foil at a high bearing number. Finally, the static characteristics under tilting conditions were analyzed. It was found that the more the rotor tilts, the more load and bearing torque generate due to the decreased film thickness gradient. These analysis methods and results might be used for coupling the thrust with the journal bearing.

ACKNOWLEDGEMENTS

This work was performed by KIST and supported by a grant from "Development of intelligent sensors & actuators for high speed rotating machinery" project of the Korea Institute of Science and Technology, "Standardization of test method for Air Foil Bearing and Turbo Blower" project of Ministry of Commerce, Industry and Energy, and "The development of a high-speed motor system" project of Korea Energy Management Corporation, Korea. The authors thank to KIST, MOCIE and KEMCO.

REFERENCES

1. Blok, H. and VanRossum, J., 1953, "The Foil Bearing-A New Departure in Hydrodynamic Lubrication," *ASLE J. Lubr. Eng.*, **9**, pp. 316–330.
2. Walowit, J. A., and Anno, J. N., 1975, Modern Development in Lubricatino Mechanics, Applied Science Publishers, London.
3. Heshmat, H., Walowit, J. A., and Pinkus, O., 1983, "Analysis of Gas-Lubricated Foil Journal Bearings," *ASME J. of Lubrication Tech*, **105**, pp. 638-646.
4. Peng, J.-P., and Carpino, M., 1983, "Calculation of Stiffness and Damping Coefficients for Elastically Supported Gas Foil Bearings," *ASME J. of Tribology*, **115**, pp.20-27.
5. Peng, J.-P., and Carpino, M., 1994, "Coulomb Friction Damping Effects in Elastically Supported Gas Foil Bearings," *Tribology Trans.*, **37**, pp. 91–98.
6. Roger Ku, C.-P., and Heshmat, H., 1993, "Structural Stiffness and Coulomb Damping in Compliant Foil Journal Bearing: Theoretical Considerations," *Tribology Trans.*, **37**, pp. 525-533.
7. Lee, N. S., Choi, D. H., Lee, Y. B., Kim T. H., and Kim, C. H., 2002, "The Influence of the Slip Flow on Steady-State Load Capacity, Stiffness and Damping Coefficients of Elastically Supported Gas Foil Bearings," *Tribology Trans.*, **45**, pp. 478-484.
8. Kim, T. H., and San Andres, L., 2005, "Heavily Loaded Gas Foil Bearings: A Model Anchored to Test Data," ASME Paper No. GT 2005-68486.
9. Bruckner, R. J., 2004, "Simulation and Modeling of the Hydrodynamic, Thermal, and Structural Behavior of Foil Thrust Bearings," Ph. D. Dissertation, Case Western Reserve University, Cleveland, OH.

10. Heshmat, C. A., Xu, D. S., and Heshmat, H., 2000, "Analysis of Gas Lubricated Foil Thrust Bearings Using Coupled Finite Element and Finite Difference Methods," *ASME J. of Tribology,* **122**, pp. 199-204.
11. Heshmat, H., Walowit, J. A., and Pinkus, O., 1983, "Analysis of Gas Lubricated Compliant Thrust Bearings," *ASME J. of Lubrication Tech.*, **105**, pp. 638-646.
12. Iordanoff, I., 1998, "Maximum Load Capacity Profiles for Gas Thrust Bearings Working Under High Compressibility Number Conditions," *ASME J. of Tribology*, **120**, pp. 571-576.
13. Iordanoff, I., 1999, "Analysis of an Aerodynamic Compliant Foil Thrust Bearing: Method for a Rapid Design,", *ASME J. of Tribology*, **121**, pp. 816-822.
14. Heshmat, H., and Shapiro, W., 1982, "Advanced Development of Air Lubricated Foil Thrust Bearings," *ASLE J. Lubr. Eng.*, **40**, pp. 21-26.
15. Dykas, B., Prahl, J., DellarCorte, C., and Bruckner, R., 2006, "Thermal Management Phenomena in Foil Gas Thrust Bearings," ASME Paper No. GT2006-91268.
16. Lee, Y. B, Park, D. J., and Kim, C. H., 2006, "Numerical Analysis for Bump Foil Journal Bearing Considering Top Foil Effect and Experimental Investigation," *Proc. 7th IFToMM International Conference on Rotor Dynamics*.
17. EL Hak, M. G., 1999, "The Fluid Mechanics of Microdevices-the Freeman Scholar Lecture," *J. Fluids Engineering*, **121**, pp. 5-33.